nature nanotechnology

ARTICLES

https://doi.org/10.1038/s41565-022-01144-x

Check for updates

# Current-driven dynamics and ratchet effect of skyrmion bubbles in a ferrimagnetic insulator

Saül Vélez[1,5]✉, Sandra Ruiz-Gómez[2,3,6], Jakob Schaab[1], Elzbieta Gradauskaite[1], Martin S. Wörnle[4], Pol Welter[4], Benjamin J. Jacot[1], Christian L. Degen[4], Morgan Trassin[1], Manfred Fiebig[1] and Pietro Gambardella[1]✉

**Magnetic skyrmions are compact chiral spin textures that exhibit a rich variety of topological phenomena and hold potential for the development of high-density memory devices and novel computing schemes driven by spin currents. Here, we demonstrate the room-temperature interfacial stabilization and current-driven control of skyrmion bubbles in the ferrimagnetic insulator $Tm_3Fe_5O_{12}$ coupled to Pt, showing the current-induced motion of individual skyrmion bubbles. The ferrimagnetic order of the crystal together with the interplay of spin–orbit torques and pinning determine the skyrmion dynamics in $Tm_3Fe_5O_{12}$ and result in a strong skyrmion Hall effect characterized by a negative deflection angle and hopping motion. Further, we show that the velocity and depinning threshold of the skyrmion bubbles can be modified by exchange coupling $Tm_3Fe_5O_{12}$ to an in-plane magnetized $Y_3Fe_5O_{12}$ layer, which distorts the spin texture of the skyrmions and leads to directional-dependent rectification of their dynamics. This effect, which is equivalent to a magnetic ratchet, is exploited to control the skyrmion flow in a racetrack-like device.**

Magnetic skyrmions are intensively investigated owing to their topological spin texture[1–5] and sensitive response to electric currents in thin-film devices[4–7]. These properties, which can be tuned by interface engineering, open unprecedented prospects for the development of skyrmion racetrack memories[4,8] and non-conventional logic devices[9,10]. Despite this surge of interest, skyrmion-based devices have so far only been realized in metallic systems.

Controlling the formation and dynamics of skyrmions in magnetic insulators (MIs) is a prerequisite for enabling low-power spintronic and magnonic applications[11–13]. Among different classes of MIs, rare-earth garnets coupled to heavy metals have opened exciting possibilities for electrically driving and detecting magnon currents over large distances[12,14,15] and for driving domain walls at high speed[16,17] due to their low damping and ferrimagnetic order. Current-driven domain wall motion in centrosymmetric MIs is possible owing to the interfacial Dzyaloshinskii–Moriya interaction (DMI)[16–20], which favours the formation of homochiral Néel walls[17]. These walls show the greatest mobility in response to the spin–orbit torques (SOTs) generated by current flow in coupled heavy metal layers[21–24]. In addition, recent measurements of the topological Hall effect in $Tm_3Fe_5O_{12}$ (TmIG)/Pt provided indirect evidence of the formation of skyrmion-like magnetic textures in thin-film MIs[20,25–27]. The possibility of varying the DMI, magnetic anisotropy, angular momentum and damping of the rare-earth garnets by altering the composition and strain engineering[19,20,25,28] makes these systems extremely appealing for tuning the properties of skyrmions[29,30].

Despite this progress, the direct imaging and current-induced manipulation of skyrmions in MIs remain to be demonstrated. We thus lack crucial information on the nucleation, current-driven dynamics and stability of skyrmions in MIs and how they compare with metallic systems. Here, we demonstrate the interfacial stabilization and current-driven motion of skyrmion bubbles in a ferrimagnetic garnet at room temperature. We provide the first insights into the skyrmion nucleation process, current-induced dynamics in the presence of pinning and thermal diffusion, skyrmion Hall angle and rectification effects. Our results demonstrate the potential of MIs to host skyrmions and tune their motion, and highlight the limitations that need to be addressed to realize efficient skyrmion devices.

## Sample design

For our study we used $Y_3Fe_5O_{12}$(YIG)/TmIG/Pt trilayers grown on (111)-oriented $Gd_3Sc_2Ga_3O_{12}$ (GSGG) with a thickness of 10, 20 and 5 nm of YIG, TmIG and Pt, respectively. Current lines were patterned in the shape of Hall bars by optical lithography and etching of Pt (Fig. 1a), leaving the YIG/TmIG layers unetched (Methods). Magnetic characterization confirmed that the TmIG and YIG layers exhibit out-of-plane and in-plane magnetic anisotropy, respectively (Supplementary Note 2), with TmIG having a smaller coercivity and remanent magnetization (Fig. 1b) compared with films directly grown on GSGG[16–18,31]. This indicates a reduction in the magnetic anisotropy of TmIG due to exchange coupling with YIG, which favours the formation of skyrmions without compromising their stability with temperature[26,29,30]. Unless otherwise specified, the YIG film was demagnetized before starting the measurements.

## Chirality and current-induced nucleation and motion of skyrmion bubbles

Figure 1c shows magneto-optical Kerr effect (MOKE) microscopy images of the field-induced magnetization reversal of TmIG, which is characterized by the nucleation and expansion of labyrinthine stripe-like domains as commonly observed in garnets

[1]Department of Materials, ETH Zurich, Zurich, Switzerland. [2]Departamento de Física de Materiales, Universidad Complutense de Madrid, Madrid, Spain. [3]Alba Synchrotron Light Facility, Barcelona, Spain. [4]Department of Physics, ETH Zurich, Zurich, Switzerland. [5]Present address: Condensed Matter Physics Center, Instituto Nicolás Cabrera, and Departamento de Física de la Materia Condensada, Universidad Autónoma de Madrid, Madrid, Spain. [6]Present address: Max Planck Institute for Chemical Physics of Solids, Dresden, Germany. ✉e-mail: saul.velez@uam.es; pietro.gambardella@mat.ethz.ch

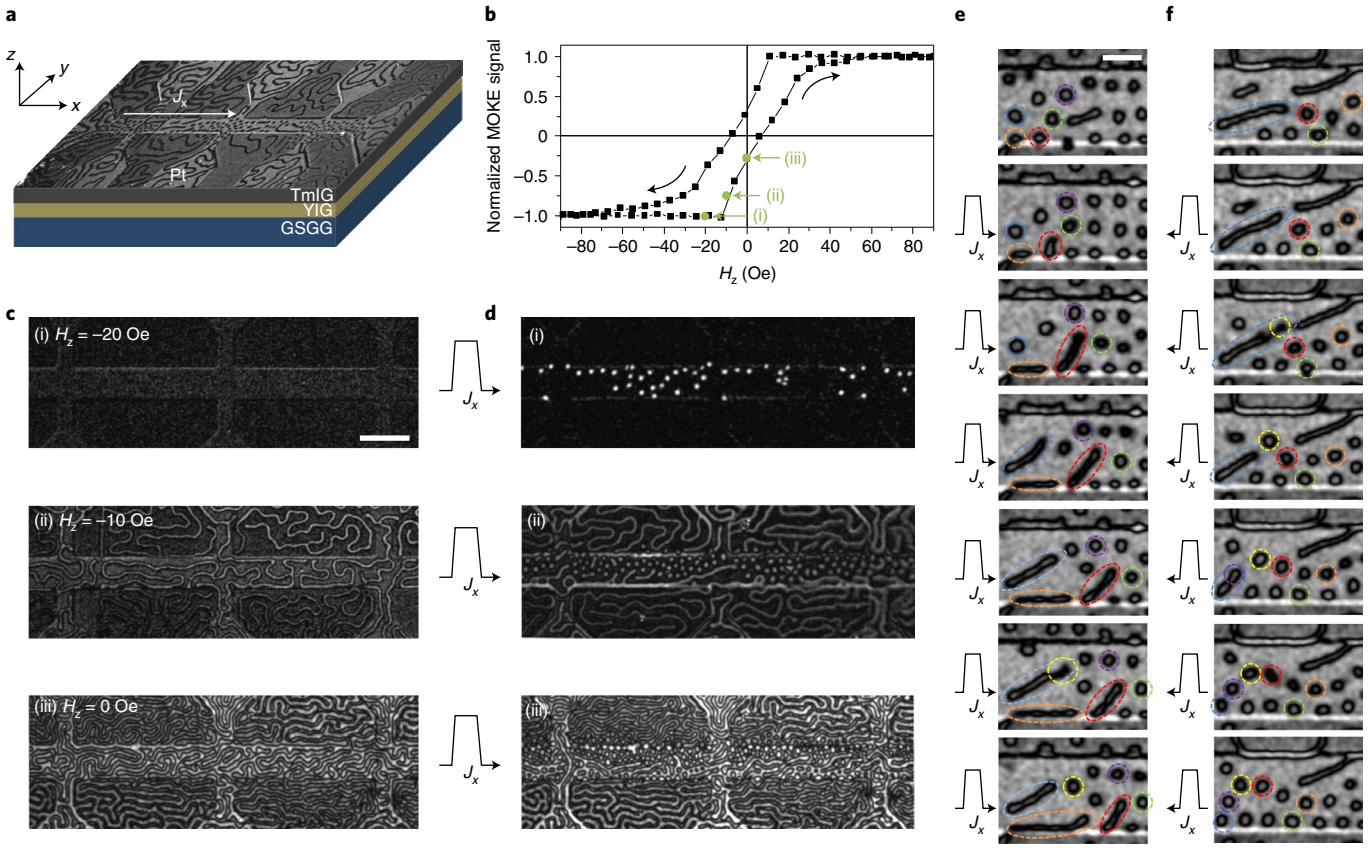


**Fig. 1 | Current-driven nucleation and dynamics of bubble domains in TmIG. a**, Schematic of the device structure with a superimposed wide-field differential MOKE image showing magnetic domains in TmIG. Bright (dark) contrast corresponds to regions with up (down) magnetization. The coordinate axis and current line are indicated. **b**, Magnetic hysteresis loop of TmIG measured by MOKE microscopy in the region covered by the current line while sweeping the out-of-plane magnetic field $H_z$. The films were first demagnetized by cycling the in-plane field in loops of alternating polarity and decreasing amplitude. **c**, Sequence of differential MOKE images collected at magnetic fields of −20 Oe (i), −10 Oe (ii) and 0 Oe (iii) (green dots in **b**) showing that the field-driven reversal of magnetization proceeds through the formation of labyrinthine stripe-like domains. Scale bar, 15 µm. **d**, MOKE images taken after the application of a current pulse $J_x = 6.2 \times 10^{11}$ A m$^{-2}$ of length $t_p = 40$ ns to the domain structures shown in **c**, revealing the nucleation of bubble domains (i) as well as the nucleation and breaking of the stripe domains into bubble domains (ii,iii). All the magnetic configurations in **c** and **d** remained stable after 1 h. The scale bar in **c** also applies to **d**. **e**,**f**, From top to bottom, sequence of MOKE images showing snapshots of the current-driven dynamics for a sequence of positive (**e**) and negative (**f**) current pulses (see arrow direction). The domains move along the direction of the current and their dynamics is influenced by pinning, resulting in the deformation of bubbles into stripes, the contraction of stripes into bubbles or the formation of new bubbles from stripes. The dashed lines in different colours evidence the position of selected domains before and after pulsing. We attribute domain motion outside the current line to repulsive dipolar interactions. The measurements were performed with $H_z = -10$ Oe, $|J_x| = 3 \times 10^{11}$ A m$^{-2}$ and $t_p = 40$ ns. Scale bar in **e**, 5 µm; the scale bar in **e** also applies to **f**.

with out-of-plane magnetization[28]. By applying a current pulse, bubble domains nucleated out of a homogeneous magnetic texture (Fig. 1d(i)) as well as from the stripe domains (Fig. 1d(ii,iii)) in the region covered by the Pt current line. These bubble domains, which have an estimated radius $R$ of 0.5–1 µm (Extended Data Fig. 1), were stable in time and were observed for magnetic fields $|H_z| \lesssim 25$ Oe, indicating that they are robust magnetic configurations. The best conditions to observe the isolated bubbles correspond to magnetic field $|H_z| = 20$ Oe, at which the magnetization is close to saturation and domains have not yet formed (point (i) in Fig. 1b). Subsequent application of current pulses resulted in the motion of both bubbles and stripe domains in the direction of the current, accompanied by the elongation or contraction of stripe domains and the nucleation of bubbles from stripe domains (Fig. 1e,f). This directional motion is the result of the current-induced SOTs that are exerted on the walls that delimit the domains[6,22,23].

According to the sign of the torques and spin Hall effect in TmIG/Pt[16,17,31], we concluded that the domain walls of both bubbles and stripes have a right-handed Néel chirality. The closed geometry of the bubbles and the chirality of the domain walls point to a skyrmionic texture[2,6], supporting previous reports of the topological Hall effect in TmIG/Pt[20,25–27]. Scanning nitrogen vacancy (NV) magnetometry measurements of YIG/TmIG/Pt (Methods) confirmed the skyrmionic nature of the bubbles. Figure 2 presents the stray field maps and reconstructed magnetization textures of a circular (Fig. 2a–c) and deformed bubble due to pinning (Fig. 2d–f). The fits of the magnetic stray field revealed a domain wall width $\Delta_{DW}$ of ~60 nm and confirmed the right-handed Néel chirality of the walls. Analysis of the stray field of the straight domains in YIG/TmIG further indicated that the right-handed Néel chirality of the walls is also favoured in Pt-free regions (Supplementary Note 3), suggesting that the YIG/TmIG interface has a positive DMI, unlike GSGG/TmIG[17]. As the top TmIG/Pt interface has a positive DMI[17], we concluded that both YIG and Pt contribute to stabilize right-handed Néel walls and skyrmions in TmIG.

The threshold DMI strength $D_{th}$ required to stabilize the chiral domain walls is given by[16,17,21] $D_{th} = 2\mu_0 M_s^2 t \ln 2/\pi^2$, where $M_s$ and $t$ are the saturation magnetization and thickness of the magnetic

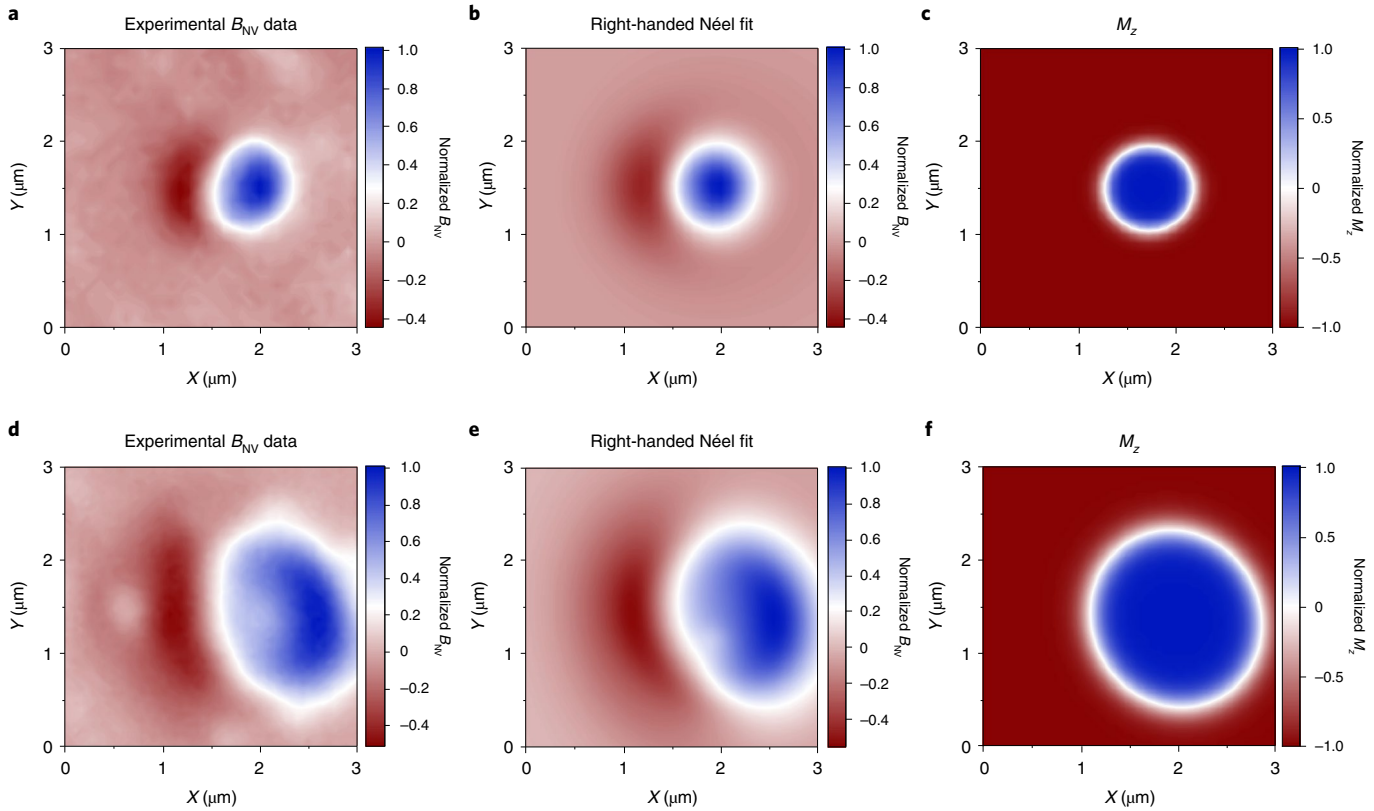


**Fig. 2 | NV magnetometry of the skyrmion bubbles in TmIG. a**, Normalized stray field map $B_{NV}(X, Y)$ of a single skyrmion bubble in YIG/TmIG/Pt measured by scanning the NV tip over the sample plane. $X$, $Y$ refer to in-plane sample coordinates. **b**, Best fit of the data in **a**, which corresponds to a circular bubble with diameter $2R \approx 950$ nm and a right-handed Néel wall with $\Delta_{DW} = 60$ nm. The bubble is assumed to exhibit an ellipsoidal shape with an arbitrary orientation in the $X$–$Y$ plane. **c**, Reconstructed out-of-plane magnetic component $M_z$ corresponding to the data in **b**. **d**–**f**, The corresponding stray field map (**d**), best fit of the data in **d** (**e**) and reconstructed out-of-plane magnetic component $M_z$ (**f**) for a deformed skyrmion bubble due to wall pinning. The best fit was obtained for a right-handed Néel wall with $\Delta_{DW} = 60$ nm and radial axes of the ellipsoid 940 and 830 nm. $H_z = -20$ Oe in **a** and **d**. See Supplementary Note 3 for details regarding the fitting procedure.

layer, respectively, and $\mu_0$ is the vacuum permeability. For our TmIG film (Supplementary Note 2), we obtained $D_{th} \approx 12\,\mu J\,m^{-2}$, a value that is compatible with the interfacial DMI found in TmIG-based heterostructures[16–19,26] ($D_{th}$ further reduces if demagnetizing fields are taken into account[32]). Interestingly, the low $M_s$ of TmIG lowers $D_{th}$ by two orders of magnitude compared with ferromagnets, evidencing the potential of ferrimagnetic garnets to stabilize chiral structures even with a weak DMI.

## Skyrmion Hall effect

Measurements of current-driven displacements of isolated skyrmion bubbles showed that they exhibit a skyrmion Hall effect[33,34] (Fig. 3), that is, a transverse deflection relative to the current. The direction of deflection depends on the magnetic polarity of the bubble's core (Fig. 3a), confirming that the skyrmion bubbles carry a topological charge[2]. Interestingly, the sign of the deflection angle $\phi_{sk}$ is opposite to that encountered in metallic ferromagnets. We ascribe the sign of $\phi_{sk}$ to the net positive angular momentum $s_{net}$ of our TmIG films, $s_{net} = -\frac{M_s}{\gamma} > 0$, where $\gamma$ is the effective gyromagnetic ratio (Methods and Supplementary Note 4). In metallic ferrimagnets, the reduced net angular momentum typically results in a small $\phi_{sk}$ (refs. [35,36]), but this is not the case for TmIG, for which the deflection angle is ~40° (Fig. 3b). In the absence of disorder, the deflection angle is given by[35] (Supplementary Note 5)

$$\phi_{sk} \approx \tan^{-1}\left(-\frac{s_{net}}{s_{tot}}\frac{2\Delta_{DW}Q}{\alpha R}\right), \quad (1)$$

where $s_{tot}$ is the total angular momentum, $\alpha \approx 0.01$ is the magnetic damping parameter[37], $\Delta_{DW} \approx 60$ nm, $R \approx 0.6\,\mu m$ (Fig. 2 and Extended Data Fig. 1) and $Q = +1/-1$ is the topological charge of a skyrmion with core magnetization pointing up/down[2]. For our films we estimated $\frac{s_{net}}{s_{tot}} \approx -0.06$ (Methods), which leads to a large $|\phi_{sk}| \approx 50°$ due to the relatively low damping of TmIG. Another remarkable difference compared with metallic systems is that, in these, pinning strongly influences the deflection angle in the vicinity of the depinning threshold, resulting in a strong dependence of $\phi_{sk}$ on the current density[33,36,38]. This is not the case for TmIG, as the average deflection angle $|\bar{\phi}_{sk}|$ is ~40° once the depinning threshold is reached (Fig. 3b). We emphasize that this result holds when averaging over several skyrmion trajectories. As discussed below, although the disorder is lower than in polycrystalline metal films, the skyrmion motion in TmIG is strongly affected by pinning and thermal diffusion.

## Skyrmion trajectories and pinning effects

We next determined whether the skyrmion trajectories are deterministic or stochastic and investigated pinning effects. Figure 4a reports the trajectories of 35 different non-interacting bubbles following the injection of a series of current pulses of density $J_x \approx 2 \times 10^{11}\,A\,m^{-2}$ (Methods). Clearly, the displacements are not linear in either time or space. Furthermore, histograms of the single-pulse displacements $\delta x$ and $\delta y$ along the $\boldsymbol{x}$ and $\boldsymbol{y}$ directions reveal a bimodal statistical distribution consisting of a narrow peak centred at $\delta x = 0$ and $\delta y = 0$, and a broader one centred at $\delta x = x_0$ and $\delta y = y_0$ (Fig. 4b). The two modes of the distribution capture pulse events that did not

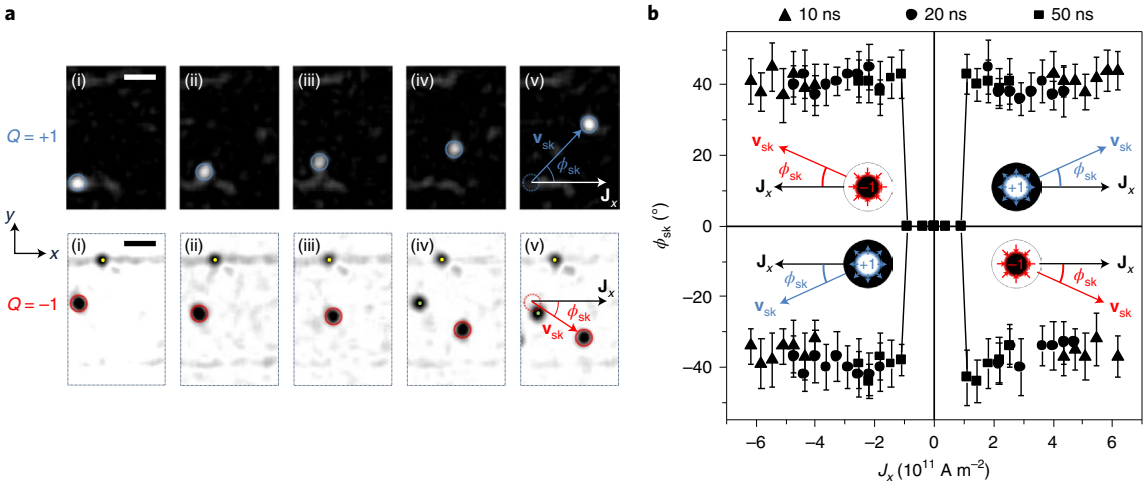


**Fig. 3 | Skyrmion Hall effect in a ferrimagnetic insulator. a**, Sequence of differential MOKE images showing the position of isolated skyrmion bubbles during a series of positive current pulses. The top and bottom images correspond to bubbles with $Q=+1$ and $Q=-1$, respectively. The direction of the current $\mathbf{J}_x$, the skyrmion velocity $\mathbf{v}_{sk}$ and the skyrmion Hall angle $\phi_{sk}$ are indicated in the rightmost image of each sequence. The images were selected from a sequence of current pulses with $J_x=2.0\times10^{11}$ A m$^{-2}$ and $t_p=20$ ns. Bright (dark) contrast corresponds to regions with up (down) magnetization. In the bottom images, the yellow spots indicate a skyrmion bubble trapped at a defect site and the green spots a bubble driven into the imaging region during the pulse sequence. Scale bars, 3 µm. **b**, Average skyrmion deflection angle $\bar{\phi}_{sk}$ measured for different amplitude, length and direction of current pulses for skyrmion bubbles with $Q=+1$ and $Q=-1$. Each data point is an average of measurements performed on ten independent skyrmion bubbles, with the error bars representing the standard deviation (Methods). Different symbols correspond to different pulse lengths. The data points with $\phi_{sk}=0$ indicate no single skyrmion depinning events. The lowest $|J_x|$ values shown for $t_p=20$ and 10 ns indicate the current threshold for skyrmion depinning at these pulse lengths. The insets show the orientation of $\mathbf{J}_x$ and $\mathbf{v}_{sk}$, the sign of $\phi_{sk}$ and the magnetic configuration of the skyrmion bubbles. $H_z=-20$ Oe (+20 Oe) for $Q=+1$ (−1).

lead to net bubble displacements (blue bars) and pulses that led to a net displacement (red bars), respectively. This behaviour indicates that the dynamics of the skyrmion bubbles driven by current pulses is strongly influenced by pinning at structural or magnetic defects. Because individual bubbles alternate between pinned and unpinned states, and because the probability of depinning is $P<1$, the skyrmion bubbles move in the creep regime[38,39].

Upon depinning, the bubbles preferentially move in the direction set by the driving force and the Magnus force (Fig. 3 and Supplementary Fig. 8). Analysis of their shape further revealed that the bubbles tend to deform in the direction of motion as well as perpendicular to it, indicating that both SOTs and the skyrmion Hall effect concur in the deformation process in the presence of pinning[35,40–42] (Extended Data Fig. 2 and Supplementary Note 7). In most cases, however, the deformation is less than 10% relative to the circular shape, and only in less than 5% of the events were clear deformations observed (Fig. 2c,f and Extended Data Fig. 2a).

The individual longitudinal and transversal displacements have standard deviations $\sigma_{x_0}$ and $\sigma_{y_0}$ that are larger than the mean $x_0$ and $y_0$ values, respectively (Fig. 4b), indicating that the net skyrmion motion is accompanied by random hopping between pinning sites. We attribute this behaviour to the influence of disorder and current-induced thermal fluctuations on the displacements[9]. Measurements of the current threshold $J_x^{th}$ for bubble depinning showed that $J_x^{th}$ decreases strongly upon increasing the pulse length $t_p$, indicating that both SOTs and thermal effects concur in the depinning process (Extended Data Figs. 3 and 4). Applying stronger currents or longer pulses results in thermal motion dominating over directional motion and in the nucleation and annihilation of skyrmions[9,43,44], which prevents us from driving the system into the flow regime as reported for metallic systems[7,34,38,41,45].

Analysis of the mean displacements revealed that the bubbles move, on average, by an amount that increases with $t_p$ (Fig. 4c,d and Extended Data Fig. 5). However, the displacements tend to finite values of $x_0\approx100$ nm and $y_0\approx70$ nm as $t_p$ drops below ~50 ns (Fig. 4c,d), which is unexpected. These values are independent of the amplitude and direction of the current as well as of the YIG magnetization (Extended Data Fig. 6). Thus, they likely reflect a characteristic length scale of TmIG, namely the average hopping distance between pinning sites. This idea is supported by the distribution of bubble deformations, which is consistent with an average distance between pinning centres of the order of 100 nm (Fig. 2d–f and Supplementary Note 7). Because the bubble radius is larger than this distance, the dynamics of the skyrmions is influenced by the pinning of the skyrmion wall to more than one pinning site. We also considered inertial and automotion effects[46,47] to explain the finite bubble displacements observed as $t_p\to0$, but these effects appear unlikely in view of the properties of our system (Supplementary Note 8).

The hopping motion has strong consequences for the mean skyrmion velocity $\bar{v}_{sk}=\sqrt{(\overline{\Delta x})^2+(\overline{\Delta y})^2}/t_p$ calculated, as is customary in skyrmion studies, using the mean bubble displacements $\overline{\Delta x}$ and $\overline{\Delta y}$ averaged over all pulses, including those that did not lead to bubble motion. As shown in Fig. 4e, $\bar{v}_{sk}$ increases from about 2 m s$^{-1}$ at $t_p>50$ ns to about 10 m s$^{-1}$ at $t_p=10$ ns. This increase is attributed to the reduced thermal load on TmIG for shorter pulses, which reduces the random hopping and leads to a more efficient directional flow of the skyrmions. Under these conditions, $\bar{v}_{sk}$ increases towards the flow regime limit, which we estimated to be ~30 m s$^{-1}$ for $J_x=1\times10^{11}$ A m$^{-2}$ (Methods). This limit, however, is hard to reach given that $J_x^{th}$ increases with decreasing $t_p$ (Extended Data Fig. 3).

It is known from experimental[33–35,38,40,43] and theoretical studies[38,39,42] that disorder strongly impacts the current-driven motion of skyrmions. Our findings reveal that the behaviour of skyrmions in a MI is remarkably different from that in metallic heterostructures. First, the density of pinning sites in TmIG, estimated from $(x_0y_0)^{-1}$ for $t_p\to0$, is ~$10^{-4}$ nm$^{-2}$, two orders of magnitude lower than in polycrystalline metal films[43]. Despite the lower disorder, the $J_x-t_p$ parameter space for skyrmion motion in TmIG is reduced to a narrow range due to current-induced heating dominating over the

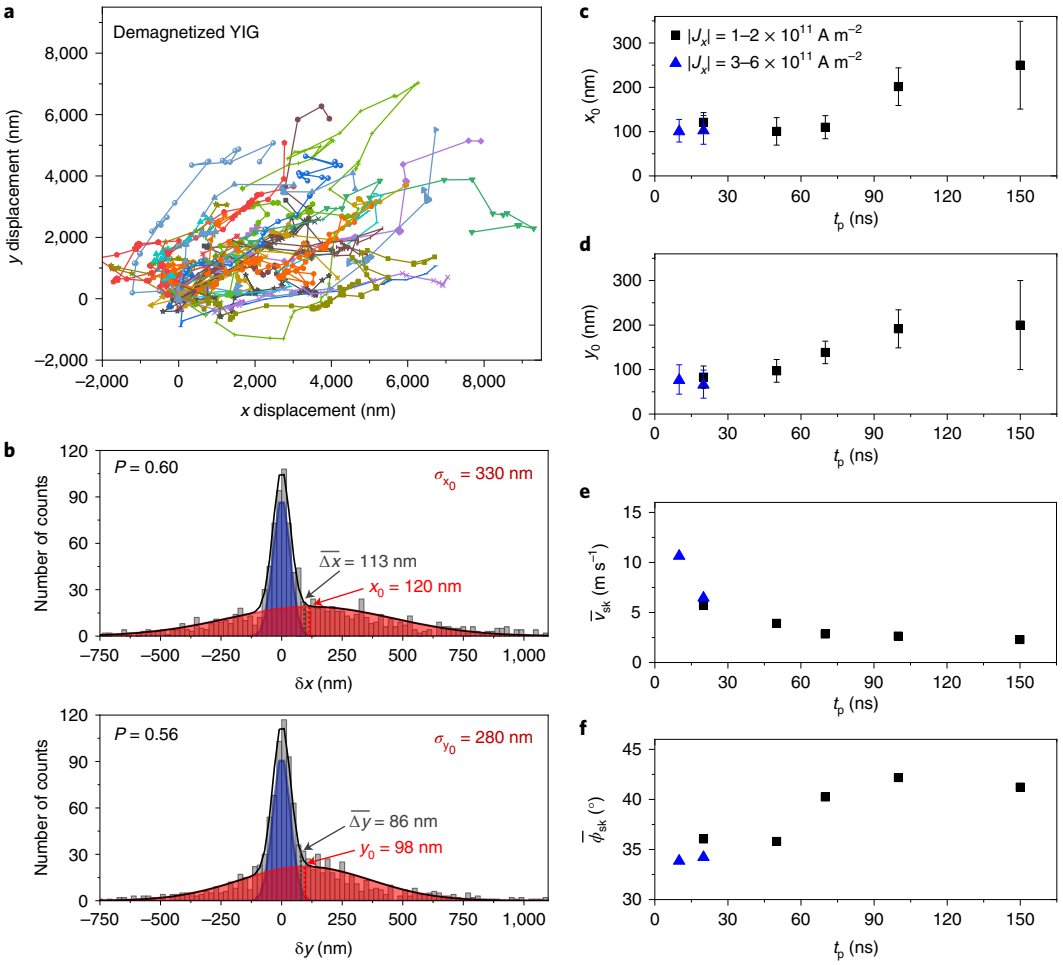


**Fig. 4 | Statistical analysis of the trajectories of skyrmion bubbles and pinning effects. a**, Representative data showing the trajectory of 35 different non-interacting skyrmion bubbles following the application of a sequence of current pulses with $J_x > 0$ and YIG demagnetized. $t_p = 50$ ns, $J_x \approx 2 \times 10^{11}$ A m$^{-2}$, $H_z = -20$ Oe and $Q = +1$. The initial position of all the trajectories is set at (0, 0), each data point represents the position of a bubble after a current pulse and each trajectory is identified by a different symbol and colour. **b**, Histograms of individual bubble displacements $\delta x$ and $\delta y$ computed as the difference in position ($x$, $y$) between adjacent data points along the trajectories shown in **a**, representing bubble displacements per pulse. The grey bars represent experimental data and the black lines the fits obtained using a double-Gaussian distribution. The blue-shaded peaks centred at $\delta x = 0$ and $\delta y = 0$ account for pulses that did not lead to bubble displacement. The red-shaded peaks capture the distribution of pulses that led to bubble motion, centred at $\delta x = x_0$ and $\delta y = y_0$, with standard deviations $\sigma_{x_0}$ and $\sigma_{y_0}$, respectively. $P$ represents the weight of the area under the red curve relative to the total histogram area. $\overline{\Delta x}$ and $\overline{\Delta y}$ are the average bubble displacements per pulse along **x** and **y**, respectively, and include all pulse events. **c**–**f**, Analysis of the skyrmion trajectories as a function of $t_p$: mean displacements $x_0$ (**c**) and $y_0$ (**d**), mean bubble velocity $\bar{v}_{sk}$ (**e**) and mean Hall angle $\bar{\phi}_{sk}$ (**f**). $\bar{v}_{sk}$ and $\bar{\phi}_{sk}$ are calculated from $\overline{\Delta x}$ and $\overline{\Delta y}$ (Extended Data Fig. 5). The error bars in **c** and **d** represent the standard errors calculated from the variance of those parameters from the double-Gaussian fit function. The blue triangles in **c**–**f** represent different current densities, as indicated in **c**.

SOTs (Extended Data Figs. 3 and 4). We attribute this limitation to the exponential dependence of skyrmion diffusion on temperature, which is expected to alter the skyrmion dynamics in materials with low damping and low disorder[9], preventing the use of currents strong enough to reach the flow regime. The thickness of our films also reduces the SOT driving force in comparison with ultrathin metallic systems[38,41,43].

Another difference with respect to metal films[33,34,38,41,43] is that the average skyrmion Hall angle $\bar{\phi}_{sk} = \tan^{-1}\left(\frac{\overline{\Delta x}}{\overline{\Delta y}}\right)$ in TmIG is very large (Figs. 3 and 4f), even though the skyrmions move in the creep regime. Theoretical models of skyrmions interacting with random point defects[39] or a granular magnetic anisotropy background[38,42,43] predict a decrease in $\bar{\phi}_{sk}$ with disorder, leading to $\bar{\phi}_{sk} \approx 0$ in the creep regime. In TmIG, however, the density of defects is low compared with in sputtered metal films, resulting in $\bar{\phi}_{sk}$ close to the flow limit given by equation (1), which only reduces from ~42° to ~34° upon $t_p$ decreasing from 100 to 10 ns (Fig. 4f). This reduction is another indication that the effects of pinning become more evident as $t_p$ is reduced. For long pulses, disorder has a small influence on the average skyrmion deflection, as inferred from the large $\bar{\phi}_{sk}$, but the thermal fluctuations are large, resulting in a reduction in $\bar{v}_{sk}$ (Fig. 4e). Conversely, for short pulses, the thermal fluctuations reduce, leading to a more efficient SOT motion, but also to a stronger influence of pinning on the trajectories of skyrmions, which results in the decrease in $\bar{\phi}_{sk}$ with decreasing $t_p$ (Fig. 4f). We also found that $\bar{\phi}_{sk}$ is nearly independent of $J_x$ (Fig. 3b), which we attribute to the competing action of SOTs and heating as $J_x$ increases above the depinning threshold. Future experimental and computational studies should aim to elucidate the influence of thermal diffusion[9] on the current-induced dynamics of skyrmions in materials with low damping and low disorder.

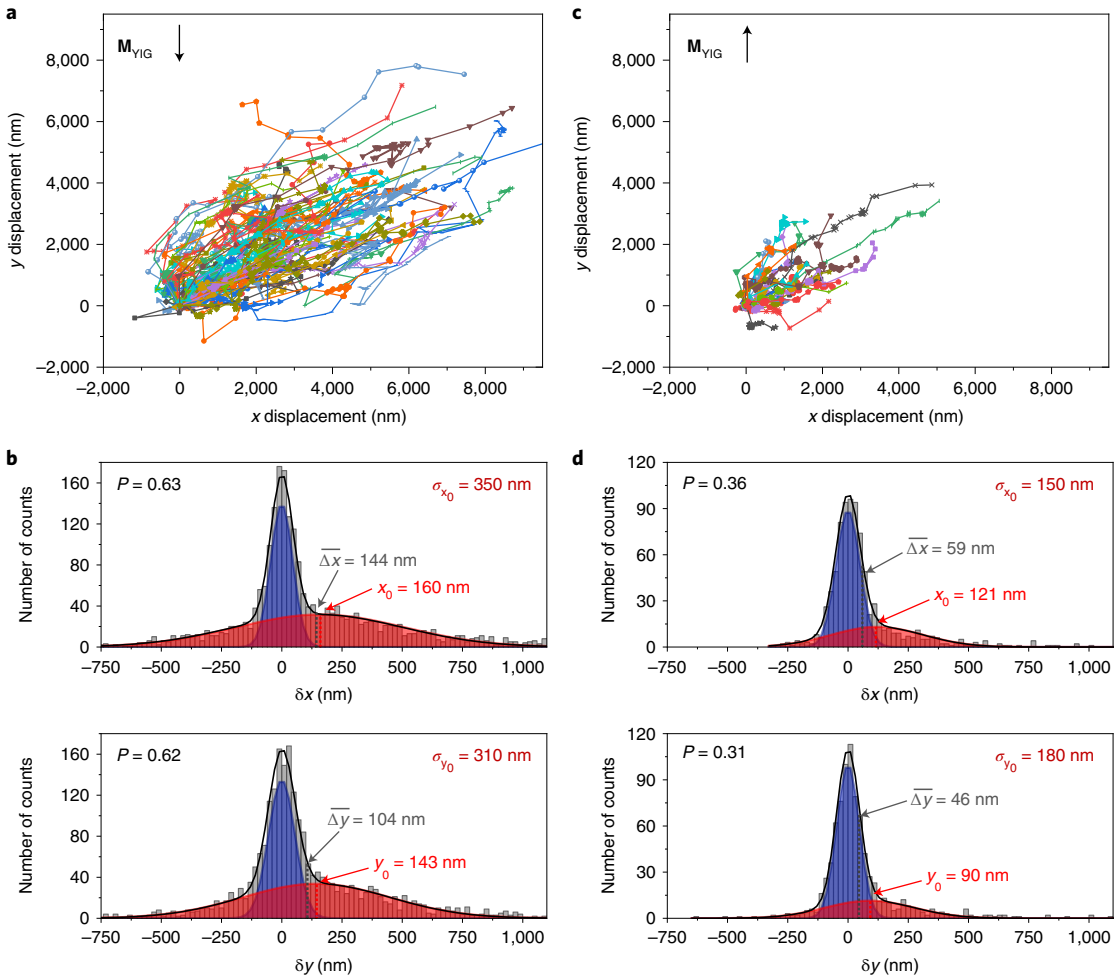


**Fig. 5 | Statistical analysis of the trajectories of skyrmion bubbles with opposite orientations of $\mathbf{M}_{YIG}$.** **a**, Representative data showing the trajectory of 68 different bubbles following the application of a sequence of current pulses with $J_x > 0$ for $\mathbf{M}_{YIG} \parallel -\mathbf{y}$. **b**, Histograms of individual bubble displacements along the **x** (top) and **y** (bottom) directions extracted from the bubble trajectories shown in **a**. **c**,**d**, The corresponding data (**c**) and histogram (**d**) for 26 bubbles and $\mathbf{M}_{YIG} \parallel \mathbf{y}$. $t_p = 50$ ns, $J_x \approx 2 \times 10^{11}$ A m$^{-2}$, $H_z = -20$ Oe and $Q = +1$. The orientation of $\mathbf{M}_{YIG}$ was set by a constant in-plane magnetic field of $|H_y| = 10$ Oe. The grey bars in **b** and **d** represent experimental data and the black lines the fits obtained using a double-Gaussian distribution, separately represented in blue and red colours, accounting for pulses that did not lead to bubble displacement and pulses that led to bubble motion, respectively (see caption to Fig. 4a,b).

## Skyrmion ratchet effect

We then investigated the influence of the in-plane magnetization of YIG ($\mathbf{M}_{YIG}$) on the skyrmion dynamics in TmIG. We found that the skyrmion trajectories are also affected by pinning in a homogeneous $\mathbf{M}_{YIG}$ and that the average deflection angle is similar for different $\mathbf{M}_{YIG}$ configurations (Figs. 4a,b and 5). However, the depinning probability and the mean bubble displacements depend strongly on the orientation of $\mathbf{M}_{YIG}$ relative to $\mathbf{J}_x$ (Fig. 5b,d). In particular, the bubble displacements with $J_x > 0$ are much larger for $\mathbf{M}_{YIG}$ directed along $-\mathbf{y}$ (Fig. 5a,b) than along $+\mathbf{y}$ (Fig. 5c,d), with the demagnetized case lying between the two (Fig. 4a,b). This asymmetry was only observed when $\mathbf{M}_{YIG}$ was perpendicular to $\mathbf{J}_x$, with the motion of the bubbles being more (less) efficient when $\mathbf{J}_x \times \mathbf{M}_{YIG} \approx -\mathbf{z}$ ($+\mathbf{z}$) regardless of their topological charge (Supplementary Table 1). These observations suggest that $\mathbf{M}_{YIG}$ modifies the probability of escape of the bubbles from the pinning potential, whereas the density of pinning sites is not substantially influenced by $\mathbf{M}_{YIG}$. We attribute this escape asymmetry to the distortion of the magnetic texture of the bubble walls induced by the exchange coupling with YIG, which results in SOTs of different strength, depending on the orientation of $\mathbf{M}_{YIG}$ relative to $\mathbf{J}_x$. The mechanism that we propose can be explained as follows. In the absence of current, the magnetic moments in the wall of a bubble ($\mathbf{m}_{DW}$) tilt towards $\mathbf{M}_{YIG}$ (Fig. 6a,b). In the presence of current, $\mathbf{m}_{DW}$ acquires an additional tilt in the direction of the damping-like SOT ($\mathbf{T}^{DL}$)[24,48], such that $d\mathbf{m}_{DW}/dt \propto -\mathbf{T}^{DL} \propto \mathbf{J}_x\mathbf{y}$ (Fig. 6c,d). Therefore, the distortion produced by $\mathbf{J}_x$ opposes (favours) the distortion induced by $\mathbf{M}_{YIG}$ when $\mathbf{J}_x \times \mathbf{M}_{YIG}$ points towards $-\mathbf{z}$ ($+\mathbf{z}$), an asymmetry that is consistent with the experiments (Fig. 5) and holds for both signs of $Q$ (Supplementary Note 10). Thus, given that $\mathbf{T}^{DL}$ controls both the depinning and the displacement of the bubbles, and that $\mathbf{T}^{DL} \propto \mathbf{m}_{DW} \times (\mathbf{m}_{DW} \times \mathbf{y})$ is proportional to the $x$ component of $\mathbf{m}_{DW}$, the skyrmion bubbles move more (less) efficiently when the magnetic tilt towards $\mathbf{y}$ is minimal (maximal). Importantly, no asymmetry in the skyrmion dynamics was observed when $\mathbf{M}_{YIG}$ and $\mathbf{J}_x$ were collinear (Extended Data Fig. 7), in agreement with our model. In addition, no changes in $\phi_{sk}$ are expected due to a change in $\mathbf{T}^{DL}$, which is also consistent with our observations (Figs. 4a and 5a,c).

We next exploited the asymmetry in the current-driven skyrmion depinning and displacements induced by $\mathbf{M}_{YIG}$ to rectify the skyrmion motion. In the vicinity of the depinning threshold, the asymmetry of $\mathbf{T}^{DL}$ induced by $\mathbf{M}_{YIG}$ leads to the unidirectional

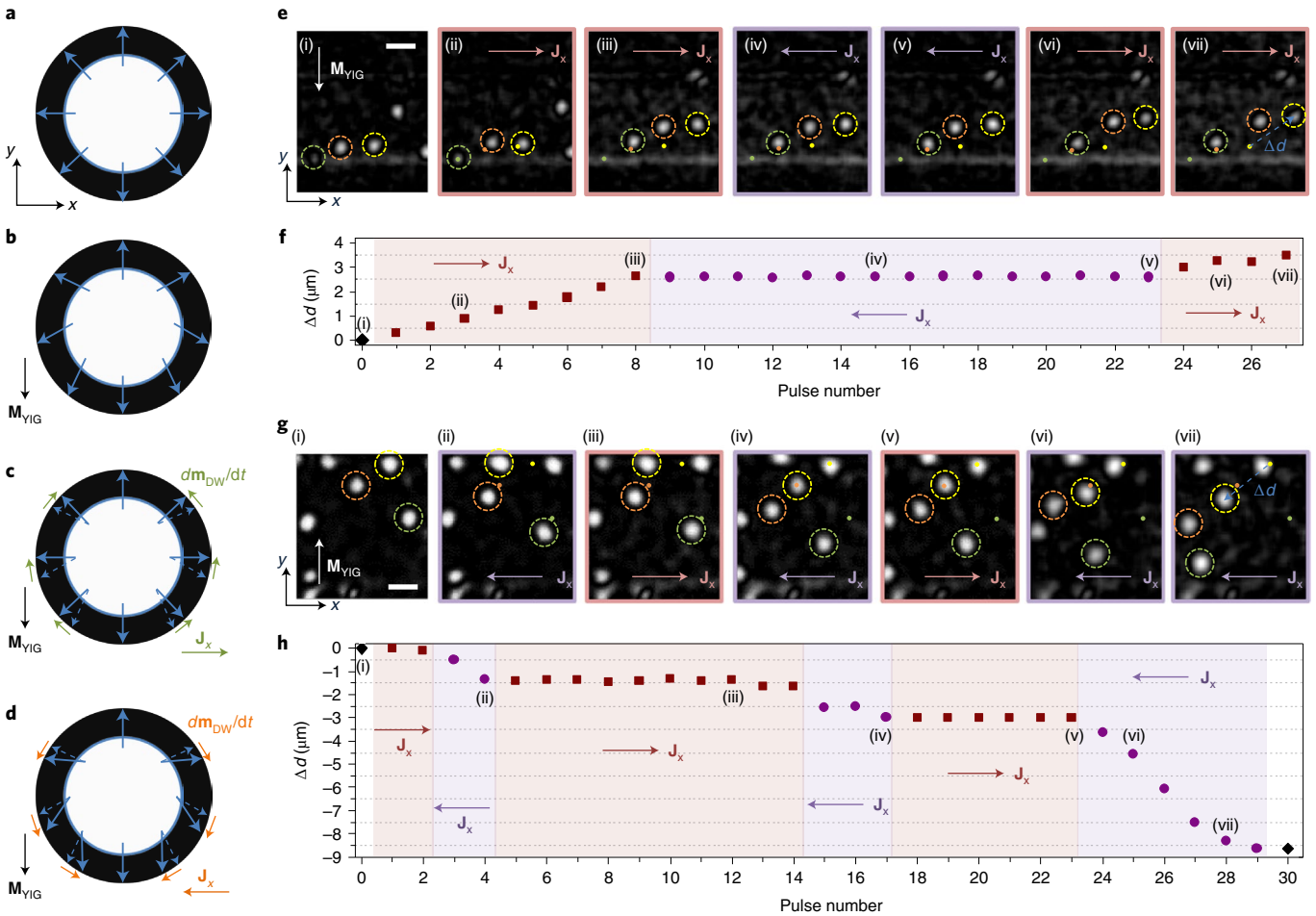


**Fig. 6 | Skyrmion ratchet effect. a**, Schematic of a domain wall's magnetic moments $\mathbf{m}_{DW}$ in a right-handed $Q=+1$ bubble. **b**, Distorted skyrmion bubble due to exchange coupling with $\mathbf{M}_{YIG}=-M_{YIG}\mathbf{y}$. **c**,**d**, Additional distortion of the skyrmion bubble shown in **b** due to the dynamic action of SOTs in TmIG/Pt as a result of currents applied in opposite directions. The dashed and solid arrows indicate $\mathbf{m}_{DW}$ before and during the pulse, respectively, with the colours green and orange indicating the direction of $d\mathbf{m}_{DW}/dt$ for opposite current directions. The reduced (enhanced) distortion of $\mathbf{m}_{DW}$ in **c** (**d**) results in a larger (smaller) current-induced driving force. **e**, Representative images showing the displacement of $Q=+1$ skyrmion bubbles following the application of a sequence of current pulses of alternating polarity with $\mathbf{M}_{YIG}$ pointing in the $-\mathbf{y}$ direction. The bubbles are highlighted by dashed coloured circles; dots indicate the initial positions of the corresponding bubbles (see image (i)). **f**, Total displacement $\Delta d=\sqrt{\Delta x^2+\Delta y^2}$ averaged for the trajectory of the three skyrmion bubbles shown in **e** (see image (vii)). The sign of $\Delta d$ corresponds to the sign of $\Delta x$. The direction of $\mathbf{J}_x$ and the image number (**e**) are indicated in the pulse sequence. **g**,**h**, Same as for **e** and **f**, but for $\mathbf{M}_{YIG}$ directed towards $+\mathbf{y}$. $|J_x|=1.8\times10^{11}$ A m$^{-2}$, $t_p=50$ ns and $H_z=-20$ Oe in **e** and **g**. The orientation of $\mathbf{M}_{YIG}$ was set by a constant in-plane magnetic field of $|H_y|=10$ Oe. Scale bar in **e**, 3 μm; scale bar in **g**, 5 μm.

motion of the skyrmions. Figures 6e,f and g,h show the trajectory of a few skyrmion bubbles for alternating sequences of positive and negative current pulses with $\mathbf{M}_{YIG}$ directed along $-\mathbf{y}$ and $+\mathbf{y}$, respectively. Clearly, the bubbles move only for one polarity of the current, which depends on the orientation of $\mathbf{M}_{YIG}$. This skyrmion ratchet effect is similar to a magnetic gate, which can be used to induce a net skyrmion displacement from random current excitations or to prevent the skyrmions moving along a particular direction when using an alternating current to generate SOTs. An analogous ratchet effect was observed for stripe domains due to the homochiral nature of the domain walls in TmIG (Supplementary Fig. 11). We note that, although the ratchet effect requires the presence of pinning, the directional asymmetry of the skyrmion motion due to $\mathbf{M}_{YIG}$ does not.

## Conclusions

We have shown that skyrmion bubbles can be stabilized and driven by proximity charge currents in a centrosymmetric MI coupled to Pt. Despite the reduced density of defects in TmIG, we found that pinning and thermal skyrmion diffusion severely affect the motion of skyrmion bubbles, which are constrained in the creep regime at currents below which thermal instabilities emerge. The bubbles move by intermittent sequential jumps between nearby pinning sites, resulting in a broad distribution of longitudinal and transverse displacements. Remarkably, the skyrmion Hall effect is large and opposite to that in ferromagnets, which we ascribe to the relatively low damping, low density of defects and positive angular momentum of the TmIG film. In principle, the ferrimagnetic order of MIs allows control of the sign and amplitude of the net angular momentum, and therefore tuning of the skyrmion Hall effect[35] and mobility[49]. Future realizations of skyrmions in MIs should aim to improve their thermal stability over a broader range of currents, possibly by a concomitant increase in the magnetic anisotropy and DMI in rare-earth garnets[19,20,25,26]. Moreover, pinning effects should be minimized to achieve deterministic and efficient skyrmion motion. Finally, we have demonstrated control over skyrmion dynamics by exchange coupling TmIG to an in-plane magnetized YIG layer. As the driving force of skyrmions depends on the

polarity of the current relative to the magnetization of the in-plane layer, it is possible to rectify the skyrmion's motion along a predefined direction. This new aspect of the skyrmion dynamics provides an additional tool for tailoring the mobility of skyrmions in spintronic devices.

## Online content

Any methods, additional references, Nature Research reporting summaries, source data, extended data, supplementary information, acknowledgements, peer review information; details of author contributions and competing interests; and statements of data and code availability are available at https://doi.org/10.1038/s41565-022-01144-x.

Received: 18 December 2020; Accepted: 2 May 2022;
Published online: 04 July 2022

## References

1. Mühlbauer, S. et al. Skyrmion lattice in a chiral magnet. *Science* **323**, 915–919 (2009).
2. Nagaosa, N. & Tokura, Y. Topological properties and dynamics of magnetic skyrmions. *Nat. Nanotechnol.* **8**, 899–911 (2013).
3. Tokura, Y. & Kanazawa, N. Magnetic skyrmion materials. *Chem. Rev.* **121**, 2857–2897 (2021).
4. Fert, A., Reyren, N. & Cros, V. Magnetic skyrmions: advances in physics and potential applications. *Nat. Rev. Mater.* **2**, 17031 (2017).
5. Back, C. et al. The 2020 skyrmionics roadmap. *J. Phys. D* **53**, 363001 (2020).
6. Jiang, W. et al. Blowing magnetic skyrmion bubbles. *Science* **349**, 283–286 (2015).
7. Woo, S. et al. Observation of room-temperature magnetic skyrmions and their current-driven dynamics in ultrathin metallic ferromagnets. *Nat. Mater.* **15**, 501–506 (2016).
8. Fert, A., Cros, V. & Sampaio, J. Skyrmions on the track. *Nat. Nanotechnol.* **8**, 152–156 (2013).
9. Zázvorka, J. et al. Thermal skyrmion diffusion used in a reshuffler device. *Nat. Nanotechnol.* **14**, 658–661 (2019).
10. Song, K. M. et al. Skyrmion-based artificial synapses for neuromorphic computing. *Nat. Electron.* **3**, 148–155 (2020).
11. Chumak, A. V., Vasyuchka, V. I., Serga, A. A. & Hillebrands, B. Magnon spintronics. *Nat. Phys.* **11**, 453–461 (2015).
12. Kajiwara, Y. et al. Transmission of electrical signals by spin-wave interconversion in a magnetic insulator. *Nature* **464**, 262–266 (2010).
13. Lebrun, R. et al. Tunable long-distance spin transport in a crystalline antiferromagnetic iron oxide. *Nature* **561**, 222–225 (2018).
14. Cornelissen, L. J. et al. Long-distance transport of magnon spin information in a magnetic insulator at room temperature. *Nat. Phys.* **11**, 1022–1026 (2015).
15. Wimmer, T. et al. Spin transport in a magnetic insulator with zero effective damping. *Phys. Rev. Lett.* **123**, 257201 (2019).
16. Avci, C. O. et al. Interface-driven chiral magnetism and current-driven domain walls in insulating magnetic garnets. *Nat. Nanotechnol.* **14**, 561–566 (2019).
17. Vélez, S. et al. High-speed domain wall racetracks in a magnetic insulator. *Nat. Commun.* **10**, 4750 (2019).
18. Ding, S. et al. Interfacial Dzyaloshinskii–Moriya interaction and chiral magnetic textures in a ferrimagnetic insulator. *Phys. Rev. B* **100**, 100406 (2019).
19. Caretta, L. et al. Interfacial Dzyaloshinskii–Moriya interaction arising from rare-earth orbital magnetism in insulating magnetic oxides. *Nat. Commun.* **11**, 1090 (2020).
20. Lee, A. J. et al. Probing the source of the interfacial Dzyaloshinskii–Moriya interaction responsible for the topological Hall effect in metal/$Tm_3Fe_5O_{12}$ systems. *Phys. Rev. Lett.* **124**, 107201 (2020).
21. Thiaville, A., Rohart, S., Jué, É., Cros, V. & Fert, A. Dynamics of Dzyaloshinskii domain walls in ultrathin magnetic films. *Europhys. Lett.* **100**, 57002 (2012).
22. Emori, S., Bauer, U., Ahn, S.-M. M., Martinez, E. & Beach, G. S. D. D. Current-driven dynamics of chiral ferromagnetic domain walls. *Nat. Mater.* **12**, 611–616 (2013).
23. Ryu, K. S., Thomas, L., Yang, S. H. & Parkin, S. Chiral spin torque at magnetic domain walls. *Nat. Nanotechnol.* **8**, 527–533 (2013).
24. Manchon, A. et al. Current-induced spin-orbit torques in ferromagnetic and antiferromagnetic systems. *Rev. Mod. Phys.* **91**, 035004 (2019).
25. Lee, A. J. et al. Investigation of the role of rare-earth elements in spin-Hall topological Hall effect in Pt/ferrimagnetic-garnet bilayers. *Nano Lett.* **20**, 4667–4672 (2020).
26. Shao, Q. et al. Topological Hall effect at above room temperature in heterostructures composed of a magnetic insulator and a heavy metal. *Nat. Electron.* **2**, 182–186 (2019).
27. Ahmed, A. S. S. et al. Spin-Hall topological Hall effect in highly tunable Pt/ferrimagnetic-insulator bilayers. *Nano Lett.* **19**, 5683–5688 (2019).
28. Hubert, A. & Schäfer, R. *Magnetic Domains: The Analysis of Magnetic Microstructures* (Springer, 1998).
29. Soumyanarayanan, A. et al. Tunable room-temperature magnetic skyrmions in Ir/Fe/Co/Pt multilayers. *Nat. Mater.* **16**, 898–904 (2017).
30. Büttner, F., Lemesh, I. & Beach, G. S. D. Theory of isolated magnetic skyrmions: from fundamentals to room temperature applications. *Sci. Rep.* **8**, 4464 (2018).
31. Avci, C. O. et al. Current-induced switching in a magnetic insulator. *Nat. Mater.* **16**, 309–314 (2017).
32. Li, H., Akosa, C. A., Yan, P., Wang, Y. & Cheng, Z. Stabilization of skyrmions in a nanodisk without an external magnetic field. *Phys. Rev. Appl.* **13**, 034046 (2020).
33. Jiang, W. et al. Direct observation of the skyrmion Hall effect. *Nat. Phys.* **13**, 162–169 (2017).
34. Litzius, K. et al. Skyrmion Hall effect revealed by direct time-resolved X-ray microscopy. *Nat. Phys.* **13**, 170–175 (2017).
35. Hirata, Y. et al. Vanishing skyrmion Hall effect at the angular momentum compensation temperature of a ferrimagnet. *Nat. Nanotechnol.* **14**, 232–236 (2019).
36. Woo, S. et al. Current-driven dynamics and inhibition of the skyrmion Hall effect of ferrimagnetic skyrmions in GdFeCo films. *Nat. Commun.* **9**, 959 (2018).
37. Crossley, S. et al. Ferromagnetic resonance of perpendicularly magnetized $Tm_3Fe_5O_{12}$/Pt heterostructures. *Appl. Phys. Lett.* **115**, 172402 (2019).
38. Juge, R. et al. Current-driven skyrmion dynamics and drive-dependent skyrmion Hall effect in an ultrathin film. *Phys. Rev. Appl.* **12**, 044007 (2019).
39. Reichhardt, C., Ray, D. & Reichhardt, C. J. O. Collective transport properties of driven skyrmions with random disorder. *Phys. Rev. Lett.* **114**, 217202 (2015).
40. Zeissler, K. et al. Diameter-independent skyrmion Hall angle observed in chiral magnetic multilayers. *Nat. Commun.* **11**, 428 (2020).
41. Litzius, K. et al. The role of temperature and drive current in skyrmion dynamics. *Nat. Electron.* **3**, 30–36 (2020).
42. Kim, J.-V. & Yoo, M.-W. Current-driven skyrmion dynamics in disordered films. *Appl. Phys. Lett.* **110**, 132404 (2017).
43. Legrand, W. et al. Room-temperature current-induced generation and motion of sub-100 nm skyrmions. *Nano Lett.* **17**, 2703–2712 (2017).
44. Woo, S. et al. Deterministic creation and deletion of a single magnetic skyrmion observed by direct time-resolved X-ray microscopy. *Nat. Electron.* **1**, 288–296 (2018).
45. Hrabec, A. et al. Current-induced skyrmion generation and dynamics in symmetric bilayers. *Nat. Commun.* **8**, 15765 (2017).
46. Torrejon, J., Martinez, E. & Hayashi, M. Tunable inertia of chiral magnetic domain walls. *Nat. Commun.* **7**, 13533 (2016).
47. Zang, J., Cros, V. & Hoffmann, A. in *Topology in Magnetism Ch. 2* (Springer, 2019).
48. Baumgartner, M. & Gambardella, P. Asymmetric velocity and tilt angle of domain walls induced by spin-orbit torques. *Appl. Phys. Lett.* **113**, 242402 (2018).
49. Caretta, L. et al. Fast current-driven domain walls and small skyrmions in a compensated ferrimagnet. *Nat. Nanotechnol.* **13**, 1154–1160 (2018).

## Methods

**Film growth and characterization.** YIG and TmIG films were epitaxially grown on (111)-oriented GSGG substrates (lattice constant $a = 12.56$ Å) by pulsed laser deposition to achieve high tensile strain (~2%) of the TmIG layer, which causes TmIG to exhibit perpendicular magnetic anisotropy, as previously demonstrated[17,50]. The properties of the heterostructure were tuned by varying the thickness of the layers and the deposition conditions. For the sample investigated in this work, the YIG film was deposited in a high-vacuum chamber at 720 °C with an oxygen background pressure of 0.15 mbar. The laser fluence was set to 0.9 J cm$^{-2}$, and the repetition rate to 2 Hz. The TmIG film was subsequently grown at 650 °C with an oxygen pressure of 0.2 mbar, and the laser fluence and repetition rate were set to 1.35 J cm$^{-2}$ and 8 Hz, respectively. After deposition, the sample was annealed at 750 °C under 120 mbar oxygen pressure for 30 min and then cooled to room temperature at a rate of −10 K min$^{-1}$ under 200 mbar oxygen pressure. To ensure a high-quality TmIG/Pt interface, the YIG/TmIG films grown were directly transferred to the sputter chamber, where the Pt layer was deposited at room temperature during 3 min at a power of 10 W in 0.05 mbar Ar plasma. The thickness of the layers was calibrated by X-ray reflectometry and determined to be 9.8, 20.2 and 5.1 nm for YIG, TmIG and Pt, respectively. The uncertainty in the garnet layers was 2.0 nm. Atomic force microscopy measurements of the surface topography showed a root-mean-square roughness of about 0.18 nm over an area of 5 × 5 μm$^2$. The films were magnetically characterized in a superconducting quantum interference vibration sample magnetometer. We estimated the saturation magnetization of TmIG and YIG to be 60 and 175 kA m$^{-1}$, respectively. See Supplementary Notes 1 and 2 for further details regarding the structural, topographic and magnetic characterization of the films.

**Device fabrication.** Hall bars (consisting of three Hall crosses separated by length $L = 50$ μm and width $W = 10$ μm) were patterned onto the Pt layer by photolithography and subsequent argon plasma etching following the method previously reported[17], leaving the YIG/TmIG films unetched. The etching time required to remove the Pt layer was calibrated using reference films. In total, 48 devices were patterned for each sample, and measurements were performed on six different samples, of which two showed skyrmion bubble stabilization and motion driven by electric currents. All the data presented in this work were acquired using the same sample. The current-induced skyrmion motion measurements were performed using the same device with the exception of the data presented in Extended Data Figs. 6 and 7 and Supplementary Fig. 9. The NV data were acquired with a third device. Additional measurements were conducted on other devices fabricated from the same sample, all showing the same characteristics. The topography of the etched structures was characterized by atomic force microscopy, from which we determined the thickness of TmIG to be reduced by ~0.5 nm as a result of the etching process, and the root-mean-square roughness in the etched region to be ~0.2 nm (Supplementary Fig. 2).

**MOKE measurements.** We used a home-built wide-field polar MOKE microscope with Köhler illumination to measure the out-of-plane component of TmIG[17]. As previously described[17], the light source consisted of a collimated light-emitting diode (Prizmatix, MIC-LED-455L) with a spectral emission characterized by a maximum peak emission at 454 nm, a centroid at 455 nm and a full-width at half-maximum of 28 nm. The set-up comprised two sets of orthogonal coils for the generation of out-of-plane and in-plane magnetic fields. For the generation of skyrmion bubbles and current-driven motion studies, current pulses were injected using an AGILENT 8114A (100 V/2 A) or Kentech RTV40 sub-nanosecond pulse generator. Impedance matching with the pulse generators was achieved by connecting a 50 Ω resistance in parallel with the Pt current line.

The magnetic contrast was enhanced by taking differential MOKE images, that is, each image was subtracted by a reference image captured in a fully magnetized state as previously described[17]. Contrast is defined as the relative brightness ratio of the differential image, being black (bright) when the difference is zero (maximal). A change in the applied magnetic field reduces the contrast due to the Faraday effect. Accordingly, the reference image for a fully down (up) magnetized state was taken at $H_z = -20$ Oe (+20 Oe). Consequently, optimized contrast was observed in the images of Figs. 1c(i),d(i), 3 and 6. Conversely, the contrast is reduced in the images in Fig. 1c(ii),d(ii) ($H_z = -10$ Oe) and Fig. 1c(iii),d(iii) ($H_z = 0$) as well as in the images of Fig. 1e,f ($H_z = -10$ Oe). For the bottom images of Fig. 3a ($H_z = +20$ Oe, $Q = -1$), the contrast was inverted to preserve the colour-code definition of black (bright) corresponding to down (up) magnetization.

For the current-driven skyrmion dynamics experiments (Figs. 3–6), the skyrmion bubbles were prepared as follows. First, we demagnetized the films by cycling the in-plane field in loops of alternating polarity and decreasing amplitude (a similar result can be obtained by cycling $\mathbf{H}_z$ instead). Second, for experiments with polarized $\mathbf{M}_{YIG}$ (Figs. 5 and 6), we then applied a field $\mathbf{H}_y$. Third, we achieved saturation magnetization of the TmIG film up (down) by applying a magnetic field of $H_z = +100$ Oe (−100 Oe), and then decreased the magnetic field to $H_z = +20$ Oe (−20 Oe). Finally, we nucleated skyrmion bubbles by applying current pulses $J_x$ of amplitude and length of $5 \times 10^{11}$ to $8 \times 10^{11}$ A m$^{-2}$ and 20 to 40 ns, respectively, resulting in an apparent random nucleation of bubbles. The amplitude, length, polarity and number of pulses were adjusted to obtain a low concentration of skyrmion bubbles (that is, less than one bubble per 5 × 5 μm$^2$ device area). Bubble nucleation, however, was favoured at defect sites[40,44] and influenced by the current-induced Oersted field. Although the latter favours bubble nucleation at the side where the out-of-plane component of the Oersted field opposes $H_z$, the presence of defects can be inferred from the preferred nucleation of skyrmion bubbles at certain positions of the device. Moreover, we observed that the skyrmions located at a few of those spots remained trapped upon the application of current pulses. Therefore, we excluded those skyrmion bubbles from the analysis of skyrmion dynamics.

For the acquisition of the skyrmion trajectories, differential MOKE images were taken at a rate of ~1 frame per pulse, with the pulses continuously applied at a repetition rate of 2 Hz. The trajectories of the bubbles were automatically determined by using the Fiji open-source software (https://imagej.net/software/fiji/downloads)[51], which allows to binarize the images and determine the position of bubble centres during the image sequence. The standard deviation of the distributions presented in blue in Figs. 4b and 5b,d, which is about 50 nm, indicates that the positions of the bubble centres can be determined with sub-100 nm resolution. However, we note that the internal structure and shape of the bubbles' walls cannot be resolved at this scale due to the optical resolution of the system, which we estimated to be ~300 nm from measurements performed on a reference sample. To evaluate the skyrmion trajectories (Figs. 3–5), only mobile bubbles separated from neighbouring bubbles by at least 5 μm were considered; in other words, we excluded from the analysis those bubbles that were permanently pinned at defect sites or that might interact with each other, as well as bubbles close to the edge of the track. For the statistical analysis, different skyrmion bubbles from different repeats and moving across different areas of the device were considered. Each data point in Fig. 3b corresponds to the average of over ten independent bubbles with the deflection angle computed from the initial and final positions of the bubbles measured after a sequence of current pulses. All the data points presented in Fig. 4c–f were extracted from the trajectory of a minimum of 50 and up to 250 skyrmion bubbles. Data collected for both polarities of $\mathbf{J}_x$ were considered for the analyses presented in Fig. 4c–f.

For the experiments reported in Figs. 5 and 6e–h, in addition to $H_z$, a permanent magnetic field of $H_y = \pm 10$ Oe was applied to keep $\mathbf{M}_{YIG}$ saturated. For fields up to $|H_y| \approx 25$ Oe, condition at which the bubble domains transform into stripe domains, the impact of $\mathbf{H}_y$ on the skyrmion dynamics was found to be negligible compared with $\mathbf{M}_{YIG}$, indicating that the ratchet effect arises from exchange coupling with YIG (see Supplementary Note 9 for more details).

**Scanning NV magnetometry.** The stray field maps of the domain walls and skyrmions in YIG/TmIG/Pt were acquired with a custom-built nanoscale scanning diamond magnetometer microscope[17]. This technique is based on a single NV defect located at the apex of a diamond tip. By scanning the tip over the $X$–$Y$ surface of a sample, one can sense the magnetic stray field $B_{NV}(X, Y)$ emanating from the surface with high magnetic sensitivity and nanometre spatial resolution, from which the spin texture of the domain walls and skyrmions can be determined[17,52–54]. Experiments were carried out in an ambient environment employing a commercial monolithic diamond probe tip from QZabre (www.qzabre.com). The spin resonance of the NV centre was monitored by optically detected magnetic resonance spectroscopy[55] using a nearby microwave antenna (~2.9 GHz) for spin excitation and fluorescence microscopy (520 nm excitation, 630–900 nm detection) for spin state readout. The orientation of the NV centre and its stand-off distance with respect to the sample surface were characterized beforehand using a reference sample, with the latter determined to be 114 ± 17 nm. Due to the relatively large stray field of the film, measurements were conducted at an additional distance of 100 nm from the surface. Although this prevented us from resolving local features below 100 nm resolution, $\Delta_{DW}$ could be reliably fitted because the domain wall profile extends over a distance that is several times larger than the domain wall width (Supplementary equation (1)). The measurements presented in Fig. 2 were collected from isolated bubble domains nucleated through the application of current pulses in the presence of a magnetic field of $H_z = -20$ Oe. The straight domain shown in Supplementary Fig. 6 was nucleated by decreasing the field to $H_z = -15$ Oe from a fully down magnetized state. The field was applied during the whole of the data acquisition. Details of the data analysis and determination of the magnetic texture of the domain walls and skyrmions are presented in Supplementary Note 3.

**Skyrmion Hall angle and velocity evaluation.** To estimate $\phi_{sk}$ and $v_{sk}$, we used the Wangsness relation[56] and set the magnetic moment and Landé $g$ factors of the tetrahedral/octahedral $Fe^{3+}$ and the dodecahedral $Tm^{3+}$ sublattices of TmIG to be $M_{s,1} = 175$ kA m$^{-1}$ and $M_{s,2} = 115$ kA m$^{-1}$, and $g_1 = 2.0$ and $g_2 = 7/6$, respectively (see refs. [57,58] and Supplementary Note 4). Accordingly, for our TmIG film, $\frac{s_{net}}{s_{tot}} = \left(\frac{M_{s,1}}{g_1} - \frac{M_{s,2}}{g_2}\right) / \left(\frac{M_{s,1}}{g_1} + \frac{M_{s,2}}{g_2}\right) \approx -0.06$. Based on previous reports[17], and considering that the magnetic anisotropy of our film is lower, we estimated the domain wall width of TmIG to be $\Delta_{DW} \approx 50$ nm. This value is consistent with the wall width inferred from NV magnetometry measurements, which was estimated to be about 60 nm (Fig. 2 and Supplementary Note 3).

The skyrmion velocity in the flow regime is given by[38,45] $v_{sk} = -\frac{1}{\sqrt{1+\eta^2}}\xi_{DL}J_x\gamma\frac{\pi R}{4}$, where $\eta = -\frac{\xi_{tot}}{\xi_{net}}\frac{\alpha R}{2Q\Delta_{DW}} \approx 0.8$, $\xi_{DL}$ is the effective field per unit current density associated with the damping-like SOT and $\gamma = g\frac{\mu_B}{\hbar}$, where $\mu_B$ is the Bohr magneton, $\hbar$ is the reduced Planck constant and $g = \frac{M_s}{\left(\frac{M_{s,1}}{g_1} - \frac{M_{s,2}}{g_2}\right)} \approx -5.4$ for our TmIG film. According to previous reports of SOT efficiency in TmIG/Pt heterostructures[16,31,59], and considering the thickness of our films, we estimated that $\xi_{DL} \approx 2\times10^{-15}\,\mathrm{T\,A^{-1}\,m^2}$ in our devices. Accordingly, we estimated $v_{sk} \approx 35\,\mathrm{m\,s^{-1}}$ for $|J_x| = 1\times10^{11}\,\mathrm{A\,m^{-2}}$ (see Supplementary Note 5 for more details).

## Data availability

The data that support the findings of this study have been deposited in the Research Collection database of the ETH Zurich and are available from https://doi.org/10.3929/ethz-b-000542503.

## References


50. Kubota, M. et al. Systematic control of stress-induced anisotropy in pseudomorphic iron garnet thin films. *J. Magn. Magn. Mater.* **339**, 63–70 (2013).
51. Schindelin, J. et al. Fiji: an open-source platform for biological-image analysis. *Nat. Methods* **9**, 676–682 (2012).
52. Tetienne, J. P.-P. et al. The nature of domain walls in ultrathin ferromagnets revealed by scanning nanomagnetometry. *Nat. Commun.* **6**, 6733 (2015).
53. Dovzhenko, Y. et al. Magnetostatic twists in room-temperature skyrmions explored by nitrogen-vacancy center spin texture reconstruction. *Nat. Commun.* **9**, 2712 (2018).
54. Gross, I. et al. Skyrmion morphology in ultrathin magnetic films. *Phys. Rev. Mater.* **2**, 024406 (2018).
55. Gruber, A. et al. Scanning confocal optical microscopy and magnetic resonance on single defect centers. *Science* **276**, 2012–2014 (1997).
56. Wangsness, R. K. Sublattice effects in magnetic resonance. *Phys. Rev.* **91**, 1085–1091 (1953).
57. Collet, M. et al. Generation of coherent spin-wave modes in yttrium iron garnet microdiscs by spin–orbit torque. *Nat. Commun.* **7**, 10377 (2016).
58. Paulevé, J. Ferromagnetic resonance of gadolinium garnet at 9300 MC/S. *C. R. Acad. Sci.* **244**, 1908–1910 (1957).
59. Ding, S. et al. Identifying the origin of the nonmonotonic thickness dependence of spin-orbit torque and interfacial Dzyaloshinskii–Moriya interaction in a ferrimagnetic insulator heterostructure. *Phys. Rev. B* **102**, 054425 (2020).


## Acknowledgements


We acknowledge A. Thiaville, A. Hrabec and C. Moutafis for useful discussions and M. Müller for technical assistance with the MOKE set-up. This work was funded by the Swiss National Science Foundation (grant nos. 200020-200465 (P.G.), 200021-188414 (M.T.), 200021-178825 (M.F.), PZ00P2-179944 (B.J.J.) and 200020-175600 (C.L.D.)), the European Research Council (Advanced Grant 694955-INSEETO (M.F.)) and ETH Zürich (Career Seed Grant SEED-20 19-2 (S.V.)). S.R.-G. acknowledges support from the Spanish Ministry of Economy and Competitiveness (FPI fellowship and grant no. RTI2018-095303-B-C53). S.V. acknowledges financial support by the Ministry of Science, Innovation and Universities through the Maria de Maeztu Program for Units of Excellence in R&D (grant no. CEX2018-000805-M) and the Comunidad de Madrid through the Atracción de Talento program (grant no. 2020-T1/IND-20041).


## Author contributions

S.V. conceived the study and coordinated the experimental work. J.S., E.G. and M.T. grew and characterized the films. S.V. fabricated the devices. S.V. and S.R.-G. performed the transport and MOKE experiments and analysed the data. B.J.J. assisted with the time-resolved transport measurements. M.S.W. and P.W. performed the NV measurements with the help of S.V. S.V. and P.G. wrote the manuscript. P.G., M.T., C.L.D. and M.F. supervised the work. All authors contributed to the scientific discussion and manuscript revisions.

## Competing interests

The authors declare no competing interests.

## Additional information

**Extended data** is available for this paper at https://doi.org/10.1038/s41565-022-01144-x.

**Supplementary information** The online version contains supplementary material available at https://doi.org/10.1038/s41565-022-01144-x.

**Correspondence and requests for materials** should be addressed to Saül Vélez or Pietro Gambardella.

**Peer review information** *Nature Nanotechnology* thanks the anonymous reviewers for their contribution to the peer review of this work.

**Reprints and permissions information** is available at www.nature.com/reprints.

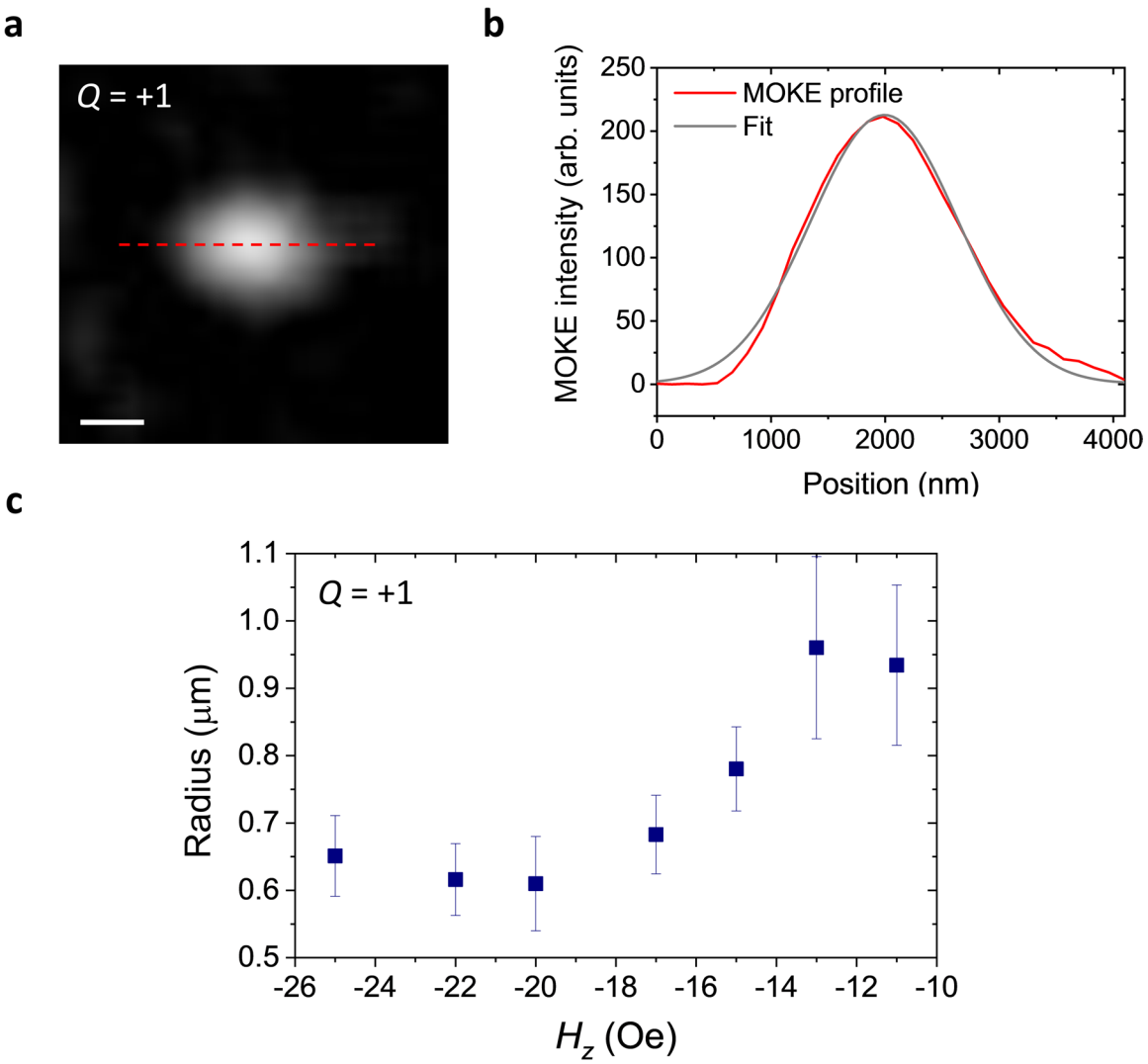


**Extended Data Fig. 1 | Skyrmion bubble radius. a**, Differential MOKE image of a representative $Q = +1$ skyrmion bubble for $H_z = -20$ Oe. The white (dark) contrast indicates regions with **m** of TmIG pointing up (down). Scale bar, 1 μm. **b**, Line profile of the MOKE intensity taken along the red dashed line in **a** (red solid line) together with its fitting (light grey) assuming that the skyrmion is a square box function having an ellipsoidal shape convoluted by a Gaussian function with standard deviation ~300 nm, which represents the spatial resolution of the MOKE set up[49]. The domain wall width, which is $\Delta_{DW} \sim 60$ nm (Fig. 2), is neglected in the fitting procedure. The main diameters $a$ and $b$ of the skyrmion bubble are extracted by fitting the two orthogonal axes of the ellipsoid. From the fit in **b** we estimate $a \sim 1.2$ μm. **c**, Skyrmion bubble radius $R$ as a function of $H_z$. The radius is estimated as $R = (a + b)/4$. Each data point corresponds to the average value obtained from fitting over 10 independent skyrmion bubbles with circular shape ($b/a \gtrsim 0.9$). The error bars represent the standard deviation of the measurements. See Supplementary Note 6 for discussion on the field dependence of the skyrmion bubble radius and bubble stabilization with $H_z$.

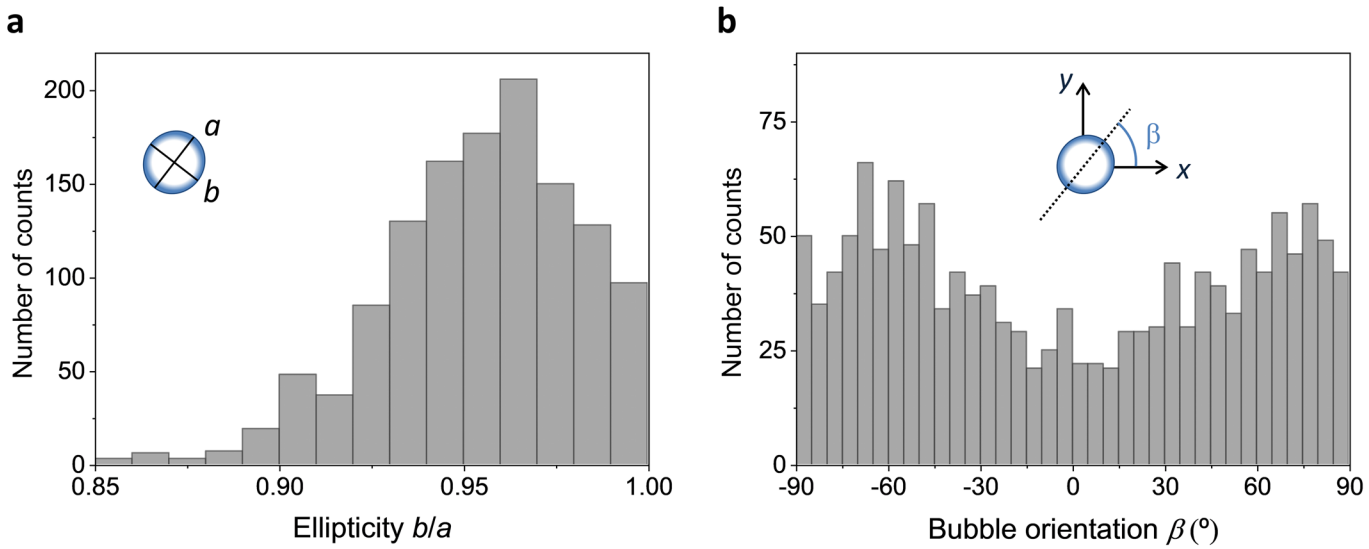


**Extended Data Fig. 2 | Skyrmion ellipticity and orientation. a**, Statistical analysis of the skyrmion ellipticity *b*/*a* from fitting over 1000 skyrmion bubbles assuming an ellipsoidal shape (see schematic). The histograms are extracted from analyzing the MOKE images of the bubble trajectories presented in Fig. 4a. **b**, Analysis of the orientation of the skyrmion ellipsoids from the data in **a**. The angle $\beta$ defines the orientation of the longest axis of the ellipsoid with respect to the current (see schematic).

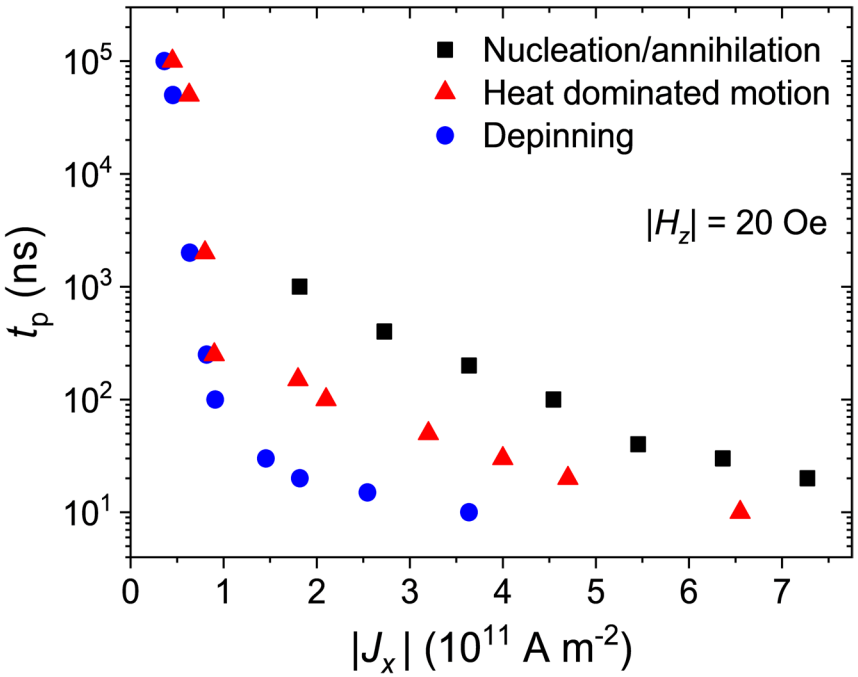


**Extended Data Fig. 3 | $J_x$–$t_p$ threshold conditions for skyrmion depinning (blue circles), heat dominated motion (red triangles), and random nucleation and annihilation of skyrmion bubbles in TmIG (black squares).** $|H_z| = 20$ Oe and the YIG layer is demagnetized. No difference was observed between $Q = +1$ and $-1$ skyrmion bubbles. Supplementary Note 9 presents the current threshold for skyrmion depinning in the presence of $\mathbf{H}_y$, that is, with $\mathbf{M}_{YIG}$ controlled with an in-plane magnetic field. All measurements of the skyrmion dynamics presented in this work were performed for $t_p$, $|J_x|$ conditions comprised between the curves defined by the blue circles and the red triangles. Above the threshold defined by the red triangles, the mean displacements $\overline{\Delta x}$, $\overline{\Delta y}$ abruptly drop, indicating that the skyrmion dynamics are dominated by Joule heating induced random skyrmion motion rather than by SOTs. We attribute this behavior to the exponential increase of the skyrmion diffusivity with temperature, which is expected in materials with low disorder and low damping such as TmIG[9].

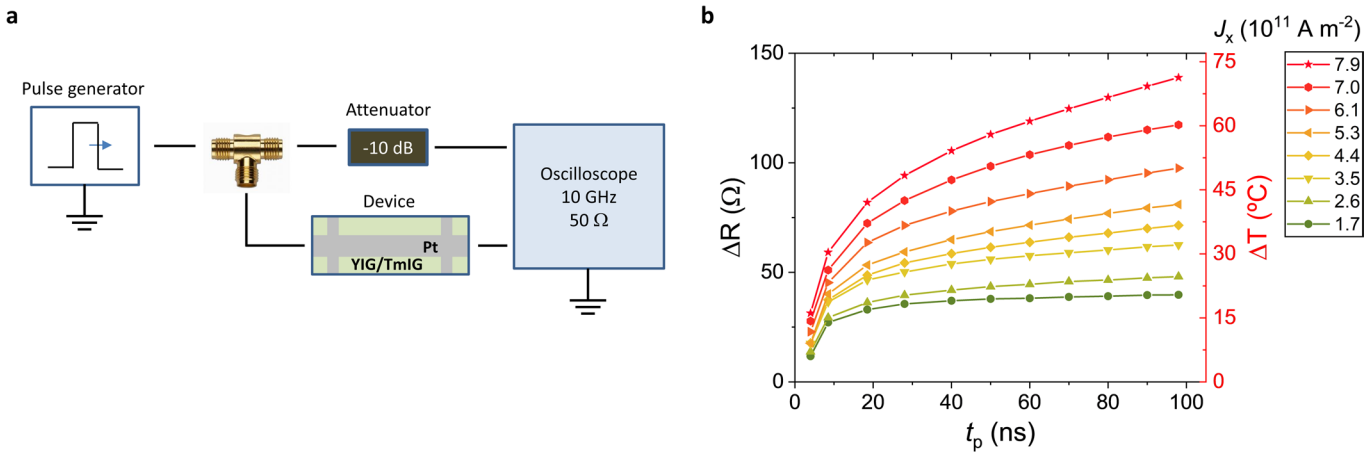


**Extended Data Fig. 4 | Current-induced temperature increase. a**, Schematic of the experimental setup. The voltage output of the pulse generator is applied through the device and both the voltage drop at the device and the pulse are monitored with an Oscilloscope with an internal impedance of 50 Ω. From these measurements, we can precisely determine the evolution of the sample resistance during the current pulse. **b**, Increase of the sample resistance during the application of a current pulse $t_p = 100$ ns (left axis). The pulse starts at time 0 ns. The colour indicates different set currents computed from the base resistance of the device $R_0(295\ \mathrm{K}) = 1130\ \Omega$. The right axis shows the increase of temperature calculated from calibration measurements. We estimate the threshold for heat dominated motion for temperature increases of about 20 K.

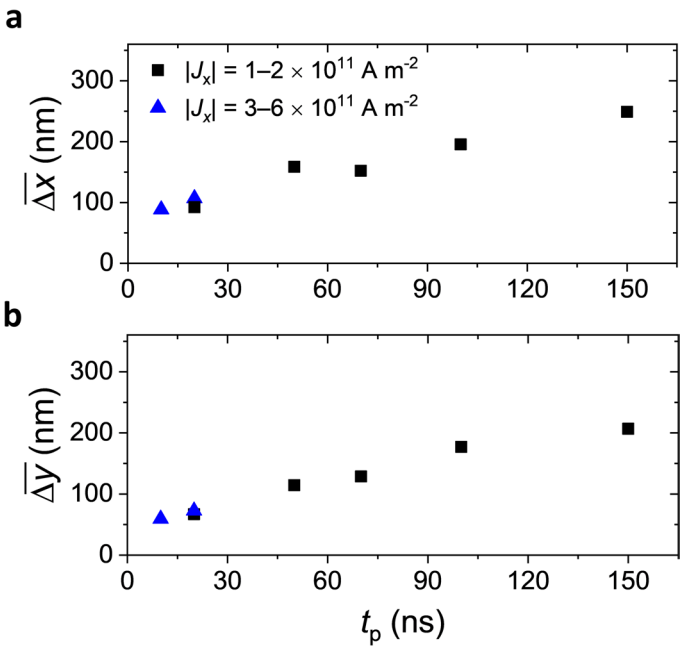


**Extended Data Fig. 5 | Mean $\overline{\Delta x}$ and $\overline{\Delta y}$ displacements for YIG demagnetized. a**, **b**, Average bubble displacements per pulse $\overline{\Delta x}$ and $\overline{\Delta y}$ as a function of $t_p$ computed considering all pulse events, that is, including those that did not lead to bubble displacements. $\overline{\Delta x}$ and $\overline{\Delta y}$ increase linearly with the pulse length, exhibiting a finite value as $t_p \to 0$. The difference between $\overline{\Delta x}$, $\overline{\Delta y}$ and $x_0$, $y_0$ (Fig. 4c,d) arises from the decrease of the bubble depinning probability when decreasing $t_p$. Different symbols indicate different current densities. $H_z = -20$ Oe ($Q = +1$). YIG is demagnetized.

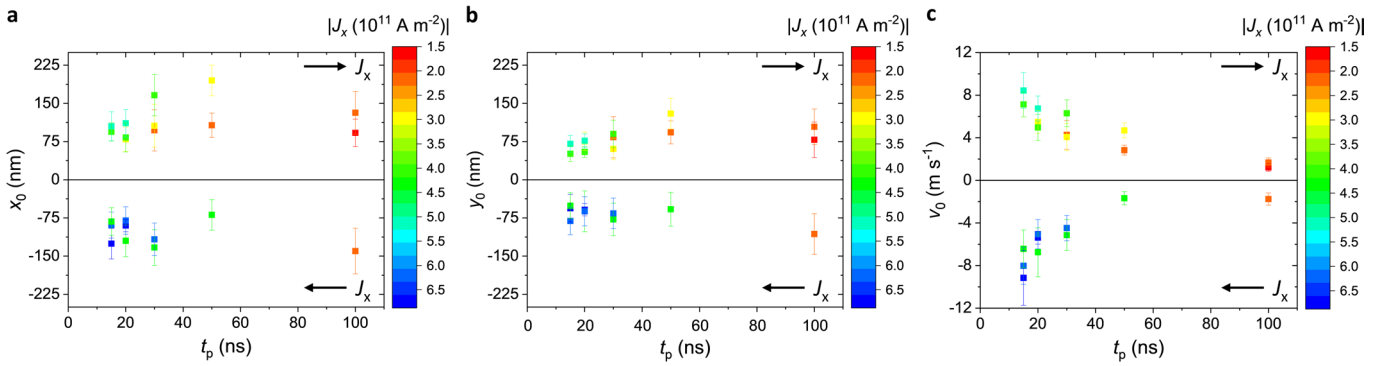


**Extended Data Fig. 6 | Pulse length dependence of $x_0$, $y_0$ with $\mathbf{M}_{YIG}$ along $-\mathbf{y}$. a**, **b**, Mean displacement values $x_0$, $y_0$ extracted from the trajectory of several skyrmion bubbles with $\mathbf{M}_{YIG}$ along $-\mathbf{y}$ (see Fig. 4a,b for details regarding the analysis). Data taken for $H_z = -20$ Oe ($Q = +1$) and for both polarities of $\mathbf{J}_x$ (indicated by an arrow). The sign of $x_0$, $y_0$ corresponds to the sign of $\mathbf{J}_x$. Different colours indicate the current density. The error bars are the standard errors of $x_0$, $y_0$ calculated from the variance of these magnitudes to the double Gaussian distribution of $\delta x$, $\delta y$. As for the case of YIG demagnetized (Fig. 4c,d), $x_0$ and $y_0$ tend to finite values when $t_p \to 0$. Remarkably, the $x_0$, $y_0$ ($t_p \to 0$) values are similar for both directions of $\mathbf{J}_x$ and similar to the ones measured for YIG demagnetized. As $t_p$ increases, $x_0$ and $y_0$ start to increase from a pulse length threshold value that depends on the amplitude of the current. Larger (smaller) current densities are required for driving skyrmion bubbles with $\mathbf{M}_{YIG}$ pointing to $-\boldsymbol{y}$ and $J_x < 0$ ($J_x > 0$), which is in agreement with the ratchet effect reported in Figs. 5 and 6 and Supplementary Note 10. **c**, Velocity of the skyrmion bubbles computed as $|v_0| = \sqrt{x_0^2 + y_0^2}/t_p$ from the data shown in **a** and **b**. The sign of the velocity is defined by the sign of $x_0$; the error bars are computed by error propagation. As observed for the mean bubble velocity $\bar{v}_{sk}$ for YIG demagnetized (Fig. 4e), $v_0$ increase as $t_p$ reduces (note that $v_0(t_p)$ exhibits a stepper increase than $\bar{v}_{sk}(t_p)$ when reducing $t_p$).

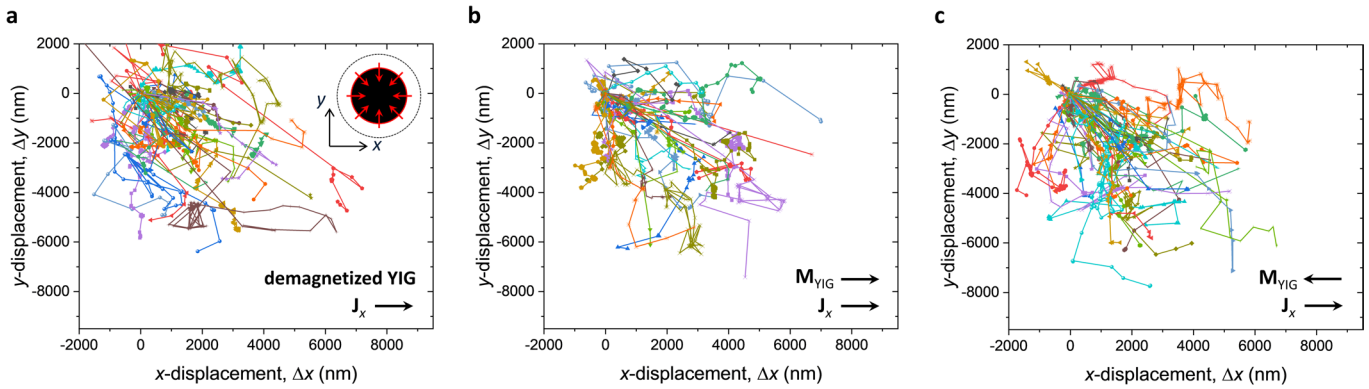


**Extended Data Fig. 7 | Skyrmion trajectories with $\mathbf{M}_{YIG}$ collinear to $J_x$.** **a**, Skyrmion trajectories with $Q$=−1 and YIG demagnetized (see inset's schematic). Data taken in a different device from the same YIG/TmIG/Pt heterostructure. $H_z$=+20 Oe, $J_x = 3.5 \times 10^{11}$ A m$^{-2}$, and $t_p$=20 ns. The measurement protocol is the same employed in Fig. 4a. **b**, **c**, Skyrmion trajectories for $\mathbf{M}_{YIG}$ pointing to **+x** and **−x**, respectively. $|H_x| = 10$ Oe. In contrast to the difference observed between $\mathbf{M}_{YIG}$ parallel to **+y** and **−y** (Figs. 5a and b), the skyrmion dynamics for $\mathbf{M}_{YIG}$ collinear with the current is, within the error, independent on the direction of $\mathbf{M}_{YIG}$. No clear differences between $\mathbf{M}_{YIG} \parallel \pm\mathbf{x}$ (**b**,**c**) and the demagnetized case (**a**) can be identified either.